Modeling and Performance Investigation on the Deformed Gas Diffusion Layer of PEM Fuel Cell

Xiangyang Chen[1], Xianglong Luo[1,*], Yingzong Liang[1], Jianyong Chen[1], Jiacheng He[1], Zhi Yang[1], Ying Chen[1], Chao Wang[1*], Yanping Du[2, 3]

(1. Guangdong Provincial Key Laboratory of Functional Soft Condensed Matter, School of Material and Energy, Guangdong University of Technology, Guangzhou, Guangdong Province, 511400, China

2. China-UK Low Carbon College, Shanghai Jiao Tong University, Shanghai, 201306, China

3.Department of Engineering, Faculty of Environment, Science and Economy, University of Exeter, Penryn Campus, Penryn, Cornwall TR109FE, UK)

Abstract

Simulation of a proton exchange membrane fuel cell (PEMFC) in its assembled state has been a long-standing challenge, with one factor being the influence of gas diffusion layer compression resulting from heat and mass transfer on the effective proton conductivity of the proton exchange membrane. Due to the lack of in-situ data, it is customary to utilize an empirical formula as a conventional model for determining the effective proton conductivity. However, significant deviations (>10%) have been observed between simulated and experimental data for fuel cells, mainly when the fuel cell is assembled. The assembly of PEMFC caused a shift of effective proton conductivity, leading to a significant deviation. To address this issue, this study proposes a model using COMSOL that integrates mechanics, electrochemistry, heat, and mass transfer of the fuel cell. To decrease the deviation between

*Corresponding authors.
E-mail addresses: lxl-dte@gdut.edu.cn (Xianglong Luo), chaowang@gdut.edu.cn (Chao Wang)

simulation and experiment, the effective proton conductivity of the proposed model is corrected by the reference proton conductivity. Specifically, an adjustment factor is introduced to the reference proton conductivity to correct the shift of effective proton conductivity caused by the compression. As a result, the average deviation of the proposed model is decreased from 10.44% to 2.25%, compared to a traditional model. As a case study, the optimal compression ratio of 20% is obtained by heat and mass transfer analysis, in which peak power density is increased from 6611.2 to 7466.6W m^{-2}. This study highlights the importance of membrane proton conductivity for the output performance of PEMFC.

Keywords: PEMFC, proton conductivity, compression ratio, gas diffusion layer, COMSOL

Highlights

- A semi-empirical model of proton conductivity caused by deformed GDL is proposed.
- The polarized curve deviation of the proposed model decreases from 10.44% to 2.25%.
- Peak power density from the proposed and previous models are 7467 and 6611 W m^{-2}.
- The optimal CR of GDL is 20% obtained by the proposed model.

1. Introduction

Due to its high efficiency, non-polluting nature, low operating temperature, and high power density, the proton exchange membrane fuel cell (PEMFC) is regarded as one of the most promising energy conversion devices for clean energy systems [1, 2]. Enhancing the power density of PEMFC is crucial for promoting and utilizing clean energy. As the PEMFC is assembled by applying a compression force to seal the system, heat and mass transfer are significantly affected by the compression of the gas diffusion layer (GDL), which has been the

subject of numerous studies [3]. It is widely known that the elastic modulus of GDL is over one order of magnitude smaller than that of other layers, such as the bipolar plate (BP), microporous layer (MPL), catalytic layer (CL), and proton exchange membrane (PEM), with values of 14, 13000, 221, 249, and 232 MPa, respectively [4]. Additionally, the compression ratio (CR), which represents the compressed volume divided by the overall volume, is typically used to evaluate the GDL strain. An increase in CR leads to greater compression of the GDL and alters its porosity, thereby affecting its permeability, diffusivity, and heat conductivity [5, 6]. The output performance of the PEMFC is closely associated with the CR. Therefore, it is important to investigate the relationship between the CR of GDL and the output performance of PEMFC.

Some researchers have employed a model to investigate the relationship between the CR of GDL and the output performance of PEMFC. For instance, Vetter et al. [7] developed a one-dimensional model of PEMFC that incorporated fields for hydrogen, oxygen, water vapor, and temperature. Zhang et al. [4] then extended this model to account for the GDL compression effects, but it did not take into account the water content of the PEM. The water content is a critical factor of PEM that impacts the output performance of the PEMFC. If the water content of the PEM falls below 4, PEM enters a drying state where the proton conductivity drops drastically, leading to a decrease in the output performance of PEMFC [8]. Kulkarni et al. [9] developed a non-isothermal model to investigate the relationship between water content and GDL compression effect, especially when CR of GDL was 15%, 25%, and 35%. They found that the water content of PEM increased when CR of GDL increased, leading to an increase in proton conductivity of PEM. Therefore, the water content of the PEM directly affects the proton conductivity of the membrane, which in turn determines the electrochemical reaction rate.

However, important parameters like the effective proton conductivity of the PEM are often overlooked or assumed to be constant, leading to significant deviations (usually >10%) in the ohmic loss region of the polarization curve [10]. Zhang et al. [4] employed an empirical formula to simulate the effective proton conductivity of the PEM, but the deviation in the ohmic loss phase was still considerable, at 7.87%. Zhang et al. [11] used an empirical formula to simulate the relationship between gas permeability and proton conductivity of the PEM. The deviation in the polarization curve was 8.71%. Yu et al. [12] used another empirical formula of effective proton conductivity to simulate the polarization curve of PEMFC, but the deviation in the ohmic loss phase was 7.01 %. Therefore, modeling investigation of PEMFC under deformed GDL needs more effort.

Despite some unresolved issues, the relationship between the CR of GDL and the output performance of the PEMFC has attracted the interest of numerous researchers [13–15]. Yim et al. [16] compared the output performance of fuel cells with 15% and 30% CR using an experiment and found that a better output performance was achieved when the CR was 30%. However, Velan et al. [17] reported that the worst output performance was obtained at a CR of 30.55% compared to the cases of 0%, 16.6%, and 22.2% CR, with the best output performance achieved at a CR of 16.6%. Moreover, Molaeimanesh et al. [18] conducted a simulation on five different CR settings (0%, 10%, 15%, 20%, and 25%) using isotropic GDL setups, which revealed that the highest current density was achieved at a CR of 15% by analyzing oxygen and steam distribution. The study also found that the compression effect does not follow a monotonic trend and that the best performance is achieved with neither too much nor too little compression [19]. However, the isotropic setup of the GDL may have led to uniform

compression without showing the distribution of heat and mass transfer under the ribs and gas channels. Heat and mass transfer behaviors under the channel and rib are different, leading to uneven temperature and species distribution. This may cause problems like localized hot spots that can damage PEMFC components. Simon et al. [20] analyzed oxygen transport and found that the best output performance occurred at a CR of 19%, but they did not consider steam distribution. Wang et al. [21] used a lattice Boltzmann theory to determine the water transfer in the different CR of 0%, 10, 20%, 30%, and 40%, respectively. They found that the part of compressed GDL leads to a low water transfer behavior compared to the part of uncompressed GDL. The steam directly affects the supply of reaction gases and the transmembrane transport of protons, which can ultimately affect the proton conductivity of PEM [22, 23]. Therefore, the output performance of the fuel cell is related to the heat and mass transfer behavior in deformed GDL.

Despite the impressive research on the impressive deformed GDL and output performance of PEMFC, the discrepancy between simulation and experimental remains substantial, indicating a challenge in predicting PEMFC output performance in deformed GDL. This study presents a semi-empirical model for the cases involving deformed GDL. To decrease the deviation of simulation and experiment in deformed GDL, the reference proton conductivity, based on the semi-empirical proton conductivity formula of PEM, is corrected by an adjustment factor. To validate the proposed model, the proposed model is solved using COMSOL, and compared to experimental data to evaluate the deviation. To evaluate the advantage of the proposed model, polarization curve, power density, effective proton conductivity, and water content of PEM are compared between the proposed and traditional models. In addition, as a

case study, the optimal CR of GDL is obtained by analyzing the distribution of gas species and temperature using the proposed model. The contributions of this study are summarized below:

- The PEMFC model, which includes mechanics, electrochemistry, heat and mass transfer, is extended to the situation applicable to the deformed GDL.
- To improve the accuracy of the model, the traditionally defined reference proton conductivity in a semi-empirical formula is corrected by a new adjustment factor.
- The deviation between the proposed model and experimental data decreased from 10.44% to 2.55% compared to the conventional model.

2.Methodology

To explore how the CR of the GDL affects the performance of PEMFC and the distribution of gas, liquid, and temperature, a two-phase, two-dimensional model is developed, incorporating GDL partitioning and anisotropic settings. The model focuses on both in-plane and through-plane directions, as shown in Fig. 1a, and uses a semi-empirical approach validated by experimental data [4]. The model also includes the solid mechanics of GDL to analyze deformation [24]. The electrochemistry of CL is used to analyze the electrical properties of PEMFCs. Furthermore, the GDL stress-strain is described by hyperelastic theory. The electrochemical reaction is analyzed using the Nernst equation and Butler-Volmer equation. The species transport in a porous medium is described by Fick's law. The heat conduction in PEMFC is described by Fourier's law. The heat convection in gas channels is described by Newton's law of cooling. The model is built and solved by COMSOL Multiphysics. A recommended range of 8%-22% (step width is 1%) for the CR of GDL is suggested to avoid irreversible damage to the GDL while ensuring effective sealing of the fuel cell [25]. Further

details on the model can be found in the Methodology section of the Supplementary Information.

Several assumptions are made in this study, which are summarized below :

- The system operates under steady-state conditions.
- Heat conduction is the primary mode of heat transfer throughout the system.
- Convective heat transfer of gas or coolant is limited to the boundary region of BP channels.
- The GDL is the only component that experiences deformation.
- The gas mixture is considered to be an ideal gas.
- Radiation heat transfer is not considered.
- The properties of all components are assumed to be isotropic, except for the GDL.

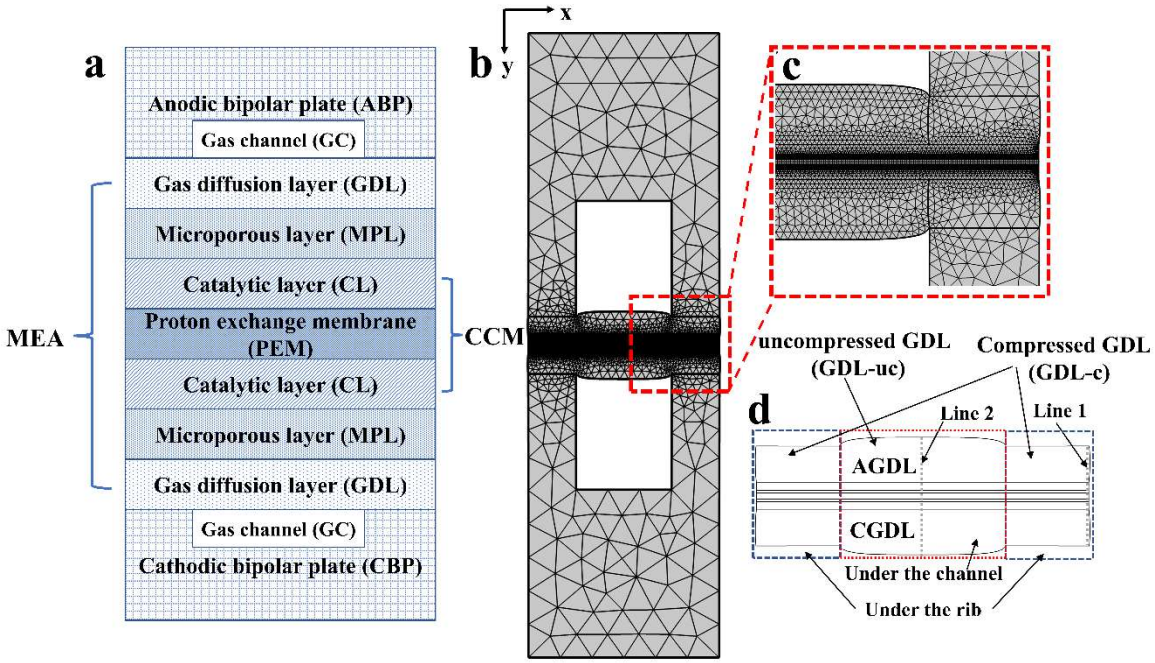

Fig. 1. Main components and meshing scheme for simulation of PEMFC. (a) Components of the PEMFC (not to scale). The prefix A means anode side, and the prefix C means cathode side. MEA is membrane electrode assembly. CCM is catalyst coated membrane. (b) Meshing scheme for simulation (to scale). (c) Meshing scheme of MEA. (d) Subdivision of the MEA

region. Line 1 is the central line through the MEA under the rib. Line 2 is the central line through the MEA under the GC.

2.1 Solid mechanic model of GDL

The GDL has small Young's moduli than the rest of the membrane electrode assembly (MEA). Due to the nonlinear relationship between stress and strain of GDL, the elastic theory is utilized to describe its stress-strain behavior [24]. The mechanical parameters relevant to this study are presented in Table S1. The conservation of volume force is expressed by Eq. (1), where P is the first Piola–Kirchhoff stress which is determined by Eq. (2); F_v is the volume force vector. The superscript T means matrix transposition.

$$0 = \nabla \cdot P^T + F_v \tag{1}$$

$$P = F \cdot S \tag{2}$$

$$F = I + \nabla u \tag{3}$$

F is the deformation gradient tensor, which is determined by Eq. (3), where I is the unit matrix and u is the displacement; S is the second Piola–Kirchhoff stress, which is described by Eq. (4); S_{inel} is the inelastic stress tensor, and W_s is the strain energy density.

$$S = S_{inel} + \frac{\partial W_s}{\partial \epsilon} \tag{4}$$

In addition, the strain energy density is determined by Eq. (5), where J_{el} is the elastic volumetric deformation; μ and λ are Lamé parameters; I_1 is the first invariant of the elastic right Cauchy–Green deformation tensor.

$$W_s = \frac{1}{2}\mu_l(I_1 - 3) - \mu_l \ln(J_{el}) + \frac{1}{2}\lambda_l[\ln(J_{el})]^2 \tag{5}$$

Subsequent calculation and analysis of the geometric models of electrochemistry, flow, heat

and mass transfer are based on the results of material mechanics.

2.2 Electrochemistry model of CL

The electrochemical reaction in low temperature PEMFC is determined by Eq. (6).

$$H_2(g) + \frac{1}{2}O_2(g) \rightarrow H_2O(l) \tag{6}$$

The reversible potential of PEMFC is described by the Nernst equation, which is formulated by Eq. (7) [26], where $\Delta G=\Delta H-T\Delta S$ is the change of Gibbs free energy during the electrochemical reaction; the reference pressure p_{ref}=1 bar.

$$\Delta\phi_0 = -\frac{\Delta G}{2F} + \frac{RT}{2F}\ln\left[\left(\frac{p_{H2}}{p_{ref}}\right) * \left(\frac{p_{O2}}{p_{ref}}\right)^{0.5}\right] \tag{7}$$

In this study, the electrochemical reaction in PEMFC is composed of a hydrogen oxidation reaction (HOR) in the ACL and an oxygen reduction reaction (ORR) in the CCL. Both reactions are precisely determined by the Butler-Volmer equation as Eq. (8), where $\alpha_{an}=\alpha_{cath}$=1.

$$\left.\begin{matrix} i_{an} \\ i_{cath} \end{matrix}\right\} = \begin{cases} i_{0,an}a_{an}\left[\exp\left(\frac{\alpha_{an}F\eta}{RT}\right) - \exp\left(\frac{-\alpha_{cath}F\eta}{RT}\right)\right] \\ i_{0,cath}a_{cath}\left[\exp\left(\frac{\alpha_{an}F\eta}{RT}\right) - \exp\left(\frac{-\alpha_{cath}F\eta}{RT}\right)\right] \end{cases} \tag{8}$$

2.3 Conservation equation of transportation of electric charge in the MEA

There are two types of charge conduction: proton conduction and electron conduction. Proton conduction involves the region of the catalyst coated membrane (CCM), while electron conduction involves all regions except PEM. In this study, Ohm's law is used to describe the charge conduction in PEMFC. Ohm's law for electrons and protons is determined by Eq. (9).

$$\begin{cases} \nabla\cdot(-\sigma_e \ \nabla\phi_e) = S_e \\ \nabla\cdot(-\sigma_p \ \nabla\phi_p) = S_p \end{cases} \tag{9}$$

The effective proton conductivity of Nafion membranes has been studied. Springer et al. [27] proposed an empirical formula which was determined by Eq. (10) in 1991. The deviation of the

polarization curve between the simulation and experiment in the ohmic loss region was >10%. In 2021, Zhang et al. [4] used it to simulate and found that the deviation of the ohmic loss in the polarization curve between the simulation and experiment was 7.87%. After years of development, the formula of effective proton conductivity was developed by Vetter et al. [7], which is determined by Eq. (11) in 2018, where T_{ref}=80°C; $\epsilon_i^{1.5}$ representing the Brugman correction for adjusting the ionomer content in the PEM and CL [28]. $\sigma_{p,ref}$ in Eq. (11) is called a reference proton conductivity in this study. However, the formula was proposed when the GDL was undeformed.

$$\sigma_p = (5.139\lambda - 3.26) \times 10^{-3} \cdot \exp\left[1268 \times \left(\frac{1}{303} - \frac{1}{T}\right)\right] \tag{10}$$

$$\sigma_p = \epsilon_i^{1.5} \ \sigma_{p,ref} \cdot \max\{0, f - 0.06\}^{1.5} \cdot \exp\left[\frac{15000}{R}\left(\frac{1}{T_{ref}} - \frac{1}{T}\right)\right] \tag{11}$$

The deformation of GDL during the operation of PEMFC causes a significant deviation in Eq. (11). Therefore, it is crucial to extend the effective proton conductivity formula to accommodate GDL deformation. Previous research by Vetter et al. [7] suggested that the 116 S m^{-1} of reference proton conductivity best fits various experimental data. However, there is limited information on the effective value of conductivity when assembling PEMFCs.

Indeed, the GDL is deformed when PEMFC is assembled, leading to the heat and mass transfer behavior change in PEMFC. The water content and temperature in PEM are changed due to the deformed GDL. Moreover, the effective proton conductivity of PEM is related to the water content and temperature [29]. Then, heat and mass transfer behavior changes cause a change in the effective proton conductivity of PEM. Slade et al. [30] used an experiment to determine the relationship between effective proton conductivity and the compression effect of PEMFC. They found that the effective proton conductivity was shifted within a range of 10%.

Harilal et al. [31] used an experiment to investigate the effective proton conductivity of PEMs, which found that the effective proton conductivity of different types of PEM was shifted within a range of 6%. Therefore, a correction of reference proton conductivity is needed for the performance prediction of PEMFC.

To expand the model to the situation of deformed GDL. This study proposes an adjustment factor, a_1, to account for the shift in proton conductivity caused by GDL deformation during PEMFC operation. The adjustment factor is used to correct the conductivity deviation resulting from the non-uniform distribution of water content in the PEM. As a result, the new reference proton conductivity is determined by Eq. (12). The value of a_1 is determined to be 1.1 based on simulation results. In addition, the effective proton conductivity of the traditional model is usually 4.2 S m^{-1} from the experimental data [32].

$$\sigma_{p,ref} = a_1 \cdot 116 \tag{12}$$

Furthermore, the volume fraction of water in the ionomer, denoted by f, can be calculated using Eq. (13), where V_m=517.76 cm^3 mol^{-1} represents the equivalent volume of the dry membrane [33]; V_w=18.40 cm^3 mol^{-1} denotes the molar volume of liquid water under typical operating conditions of PEMFC.

$$f = \frac{\lambda V_w}{\lambda V_w + V_m} \tag{13}$$

The Supplementary Information details the phase transitions, heat and mass transfer, and source terms.

In a word, the heat and mass transfer behavior is changed by the deformed GDL, leading to the shift of effective proton conductivity. Therefore, correcting the reference proton conductivity to decrease the deviation between simulation and experiment is necessary.

Specifically, when assembling PEMFC, a pre-tightening force is required to match each component and seal the whole system. The GDL is easily deformed due to its low Young's moduli. Therefore, the solid mechanic model of GDL in section 2.1 is used to describe the GDL deformation. The electrochemistry, heat and mass transfer simulation is based on the GDL deformation. In addition, the electrical potential and current of PEMFC are determined by the Butler-Volmer formula, as shown in Eq. (8). The potential is related to the Galvanni potential difference, as shown in Eq (S7). Moreover, the potential difference is related to temperature, gas pressure, and Gibbs free energy, as shown in Eq. (7) and Eq. (S8). In charged particle transport, Ohm's law is used to describe the reaction rate and conductivity of electrons and protons, as shown in Eq. (9). The effective proton conductivity is related to the reference proton conductivity, temperature, and water content of PEM, as shown in Eq. (11)-(13).

3. Results and Discussions

3.1 Mesh independence and model validation

Fig. 1b and 1c illustrate five different mesh configurations for the membrane electrode assembly (MEA) region, and the current density for each configuration at U=0.5 V is computed for comparison. Table 1 presents the primary boundary conditions and parameters [4]. The results obtained for 353.15 K operating temperature, 80% gas relative humidity (RH), and 0.5 V output voltage are tabulated in Table 2. The relative error of current density between scheme M4 and scheme M5 is lower than 0.27%, the simulated result of using scheme M4 has little impact on the calculated accuracy. To balance the simulation accuracy and operation time of the model, scheme M4 with 13773 elements is adopted for the subsequent simulations.

Table 1. Main boundary conditions and parameters.

Parameter	Value
Operating conditions	
Pressure of gas / kPa	200
Relative humidity	80%
Temperature of gas / K	353.15
Faraday constant / C mol^{-1}	96485
Universal gas constant / J mol^{-1} K^{-1}	8.314
Temperature of surrounding / K	353.15
Thermal and transport parameters	
GDL permeability without compression / m^2	1.23×10^{-11}
MPL permeability / m^2	10^{-13}
CL permeability / m^2	10^{-13}
Porosity of the GDL without compression	0.76

Fig. 2 compares the simulation results in the present study and the experimental results considering a_1 as 1.1. The comparison shows that the average deviation between the simulated and experimental data, considering the GDL strain, is 2.25%. In addition, the average deviation of the polarization curve between the data from the traditional model simulation and experiment is 10.44%. Therefore, the proposed model is more reliable than the traditional model.

Table 2. Calculation results.

Mesh schemes	Number of cells	Current density / A cm^{-2}	Calculation time / s

M1	5493	1.4794	36
M2	7341	1.4796	47
M3	10565	1.4586	75
M4	13773	1.4471	106
M5	16204	1.4433	129

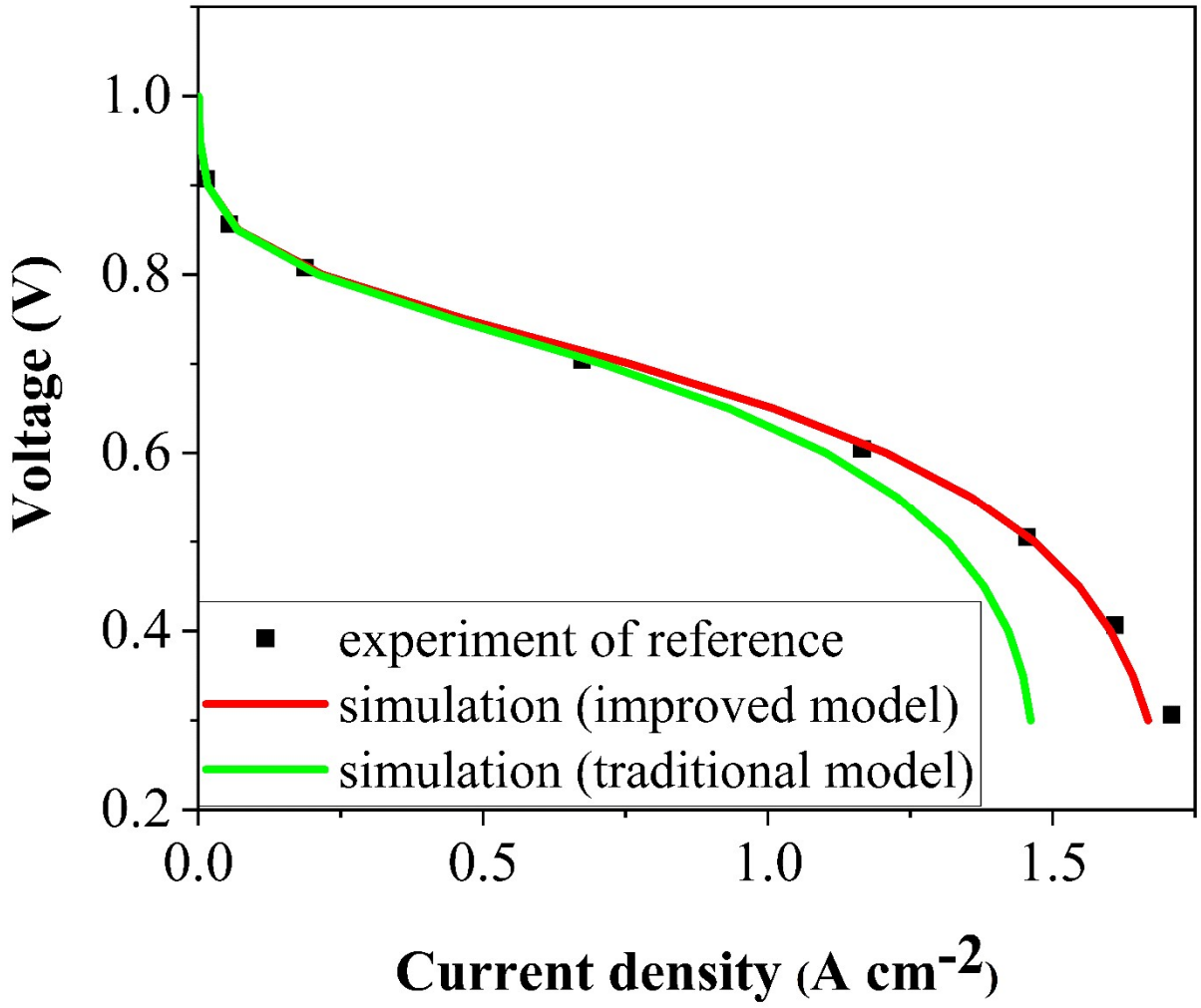

Fig. 2. Comparison of the simulated and experimental data [4].

3.2 Power density and polarization curves of PEMFC

To demonstrate the performance of PEMFC under different operational conditions, three output voltages (0.8 V, 0.6 V, and 0.4 V) are selected to represent low current density (LCD), medium current density (MCD), and high current density (HCD), respectively. A voltage of 0.8 V is the starting point of the ohmic loss stage, which is typically used as the initial voltage for the fuel cell. A voltage of 0.6 V is considered the standard operating condition of the fuel cell and serves as the midpoint for flexible output adjustment. The voltage of 0.4 V represents a significantly flooded condition and is used to investigate the performance of the transfer under flooding. To ensure seal performance without damaging the structure, a GDL from Toray company with a CR of 8-22% is used in this study [25].

The evaluation of PEMFC performance typically involves analyzing the polarization curve and power density. In this study, as depicted in Fig. 3a and Fig. S1, the current density of the PEMFC for various values of CR, ranging from 0% to 8%-22% (in increments of 1%), is examined. Results indicate that compressed GDL (GDL-c) outperforms uncompressed GDL (GDL-uc) in terms of both current and power densities, which is consistent with previous research [34, 35]. The maximum power density is observed at CR=20%, while the minimum is at CR=0 for all CR values studied. Fig. 3b illustrates the polarization curves and power densities for CR=0 and CR=20%. Interestingly, the power density at CR=20% is higher than that at CR=0, by 4.19% (at U=0.8 V), 11.19% (at U=0.6 V), and 13.68% (at U=0.4 V). These findings suggest an optimal CR associated with peak power density within the CR range. Furthermore, the peak power density at CR=20% is 11.89% higher than that at CR=0 (represented by the black and red points in Fig. 3b), indicating that increasing CR results in a higher peak current density for the PEMFC.

According to calculated results, the peak power density when CR=20% in the proposed and traditional model are 7466.6 W m^{-2} and 6611.2 W m^{-2}, respectively. This indicates that the proposed model is effective in predicting the output performance of fuel cells.

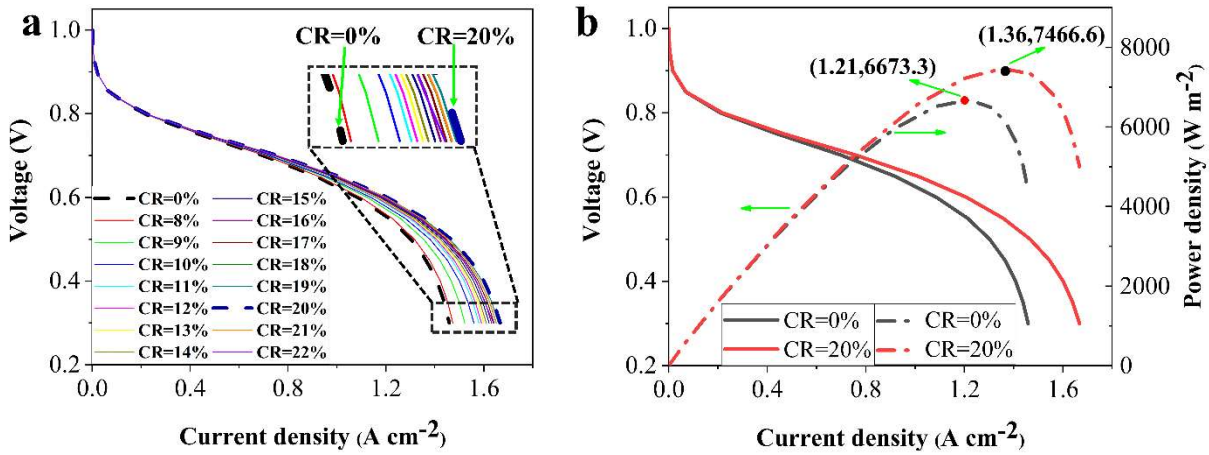

Fig. 3. Polarization curves and power densities. a) Polarization curves of CR=0, 8%-22%. b) Polarization curves and power densities for CR=0 and CR=20%.

3.3 Distribution of water content in the ionomer of CCM

Ionomers are not exclusively present in PEMs; but also in CLs, whose primary function is to transport hydrogen ions. The water content of ionomers in CCL is associated with the reaction rate, such that an increase in the reaction rate prompts an increase in the water content of ionomers in CCL. In the conventional model, the water content of PEM remains constant as the effective proton conductivity is set constant. Fig. 4 shows the average water content and effective proton conductivity of PEM in the proposed and traditional model when CR is 20%. The average water content and effective proton conductivity of PEM of the proposed model are 34.29% and 41.45% higher than that of the traditional model, respectively, indicating the proton transfer performance achieved from the proposed model is better than that achieved from the

traditional model.

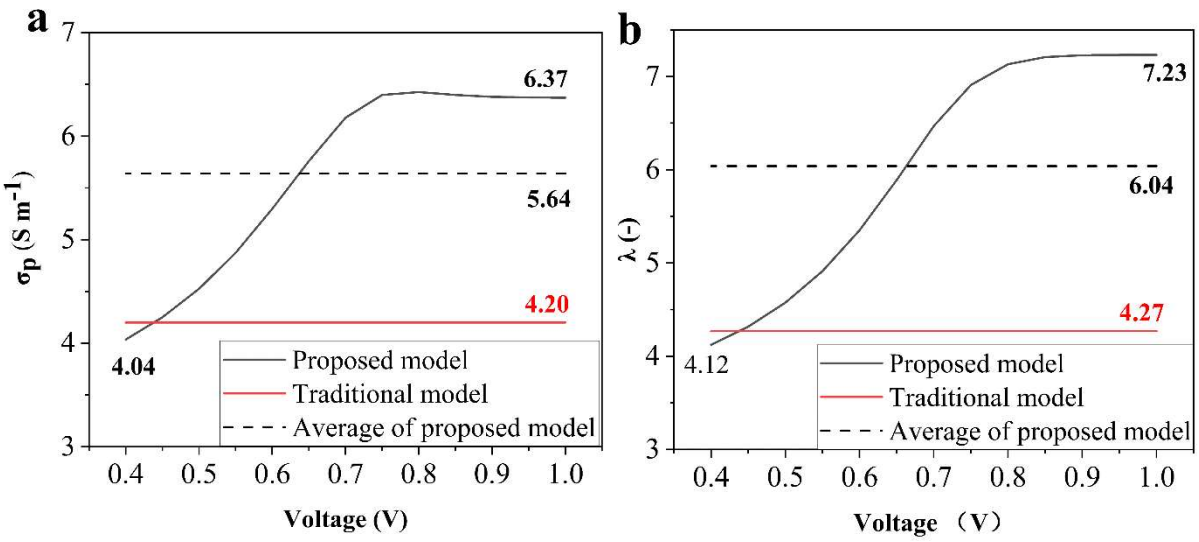

Fig. 4. Average a) effective proton conductivity and b) water content of PEM of the proposed and traditional model.

In addition, Fig. 5 gives the water content of ionomers in CCM. According to Fig. 5a and 5b, the water content of ionomer under the rib is lower than that under the GC. In comparison, the ionomer water content in the CCL/CMPL interface under the rib is higher than that under the GC. This indicates that the region is flooded as the electrochemical reaction increases. In Fig. 5c and 5e, the slope of MCD (red line) and HCD (blue line) is steeper than that of LCD (black line). This can be attributed to two factors: an increase in current density leads to an increase in the gradient of water content in the PEM, and membrane drying ($\lambda<4$) occurs at HCD, as previously reported [8]. One possible explanation is that an HCD requires a significant passage of hydrogen ions through the PEM, leading to insufficient steam supply on the anode side and subsequent drying out of the PEM. Membrane drying, in turn, exacerbates the transmembrane

transport performance.

In Fig. 5, the state of membrane drying in the through-plane region of the PEM when CR=0 and CR=20% is 46.0% and 43.2%, respectively. This shows that the dry region of the membrane is reduced at the GDL-c with the same output voltage. This suggests that the concentration loss of GDL-c is lower than that of GDL-uc, and as a result, the lifespan of the PEM in GDL-c is greater than that in GDL-uc for the range of CRs examined in this study. Typically, the anode and cathode sides of a fuel cell are humidified equally. However, when operating under HCD (low output voltage), the humidification of the reactant gas on the anode side must be calculated separately from that of the cathode side.

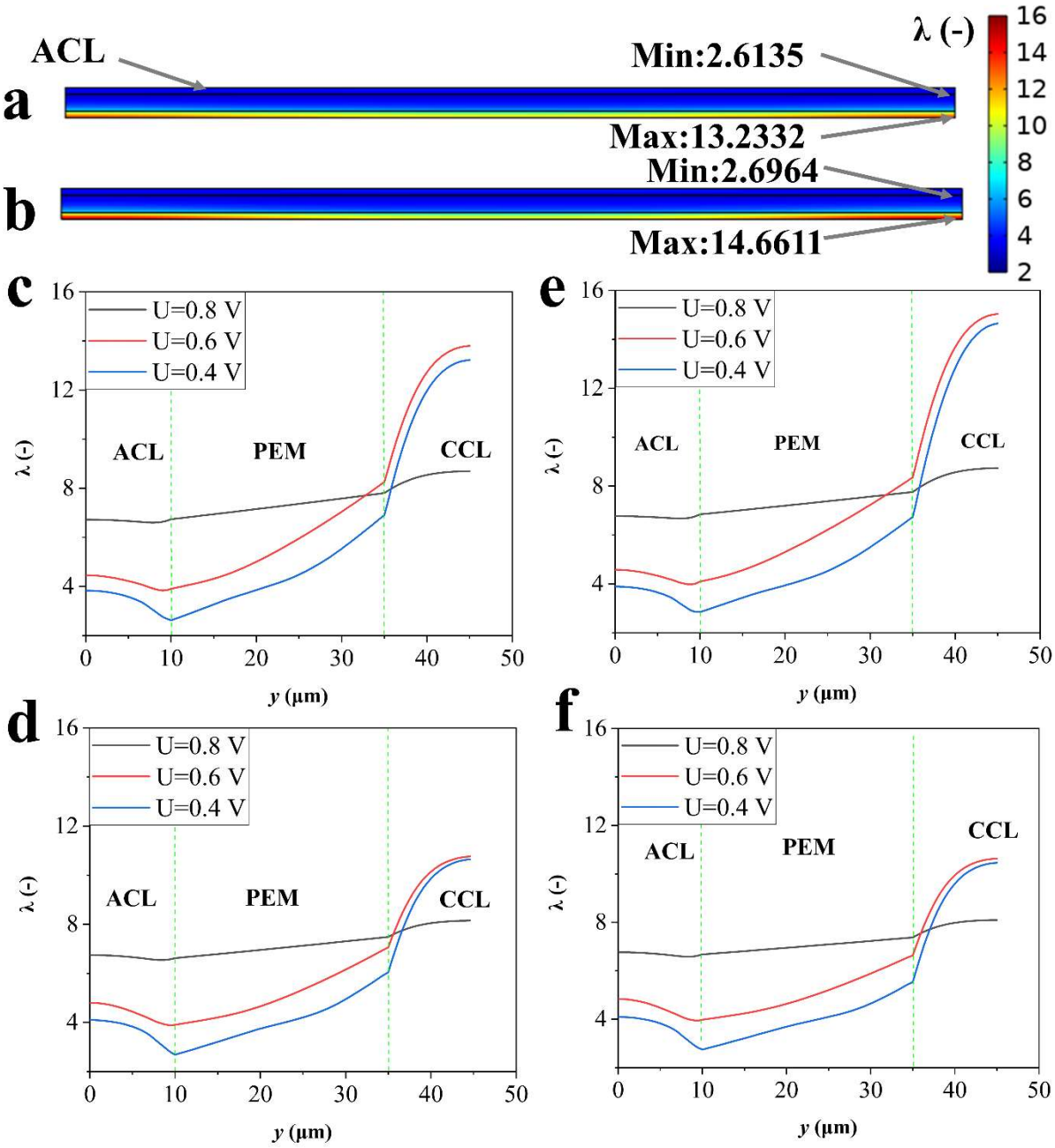

Fig. 5. Water content of ionomers in CCM at a) CR=0 and b) CR=20%. Water content distribution in Line 1 of the CCM at c) CR=0 and e) CR=20%. Water content distribution in Line 2 of the CCM at d) CR=0 and f) CR=20%.

3.4 Gas distributions of GDM

The impact of gas mass transfer on PEM water content is considered in this study by

considering gas distribution in the Gas Diffusion Media (GDM). The gas under investigation includes hydrogen, oxygen, and steam. Mole fraction is a typical representation of gas distribution behavior, which depends on mass transfer in the porous media. Optimal gas supply is crucial for achieving high power density in PEMFC, and therefore, gas distribution within the GDM is a critical factor in determining output performance. A comparison between CR=0 and CR=20% cases is presented.

3.4.1 Mole fraction of hydrogen and oxygen

Fig. 6 gives the mole fraction of hydrogen and oxygen in GDM. Due to the limited space, only the maximum value is labeled in Fig. 6c, 6f, 6i, and 6l, respectively. As shown in Fig. 6a-6c, the hydrogen mole fraction at the center of the ACL under the ribs is lower than that under the GC, which can be attributed to the longer mass transfer path length under the ribs. Furthermore, Fig. 6d-6f show the mole fraction of hydrogen at CR=20%. Even at HCD (U=0.4 V), the difference in hydrogen mole fraction is minimal. This is because hydrogen has a smaller molecular size than water and oxygen, resulting in a higher diffusion rate in porous media. Table 3 displays the average hydrogen mole fraction in AGDM for CR=0 and CR=20%, indicating that they are almost equal with a difference of less than 0.55%. Likewise, the average hydrogen mole fraction under the rib in GDL for CR=0 and CR=20% is also nearly the same, with a difference of less than 1.13%. Therefore, in most scenarios, the influence of hydrogen mole fraction on the performance of PEMFC is relatively lower compared to that of oxygen and water.

The lower mole fraction of oxygen under the rib compared to that under the GC can be attributed to three main factors: the input concentration of oxygen is lower (mole fraction =

21%) than that of hydrogen (mole fraction > 99.99%), oxygen has a larger molecular size and smaller diffusion coefficient than hydrogen, and there is a longer mass transfer distance under the rib than under the GC. According to Fig. 6, in the HCD (U=0.4 V), the molar fraction of oxygen at the CCL is 2.67% for the molar fraction of oxygen at the GC, leading to oxygen deficiency at all times during fuel cell operation. As a result, the fuel cell operates in a starved state and further increases in current density lead to severe concentration polarization or concentration loss. Table 3 presents the average mole fraction of oxygen in CGDM at CR=0 and CR=20%, with Fig. 6j-6l providing further detail. The data in Table 3 reveals that at CR=20%, the average mole fraction of oxygen in CGDM is lower by 0.68% (U=0.8 V), 7.55% (U=0.6 V), and 12.20% (U=0.4 V) compared to CR=0. These results imply that the reaction rate is higher when CR=20%, indicating a significant impact of GDL compression on the oxygen transfer performance in PEMFC. Moreover, the deformed GDL enhances the reverse osmosis of water, increasing the water content of the PEM.

Table 3 presents the mean mole fraction of oxygen in GDL under the rib, indicating that the oxygen concentration at CR=0 is greater than that at CR=20%. This disparity may be due to the lower oxygen permeability in GDL-c compared to GDL-uc, or the higher reaction rate of CR=20% relative to CR=0. Usually, the oxygen supply is the dominant factor governing the peak output performance of a PEMFC.

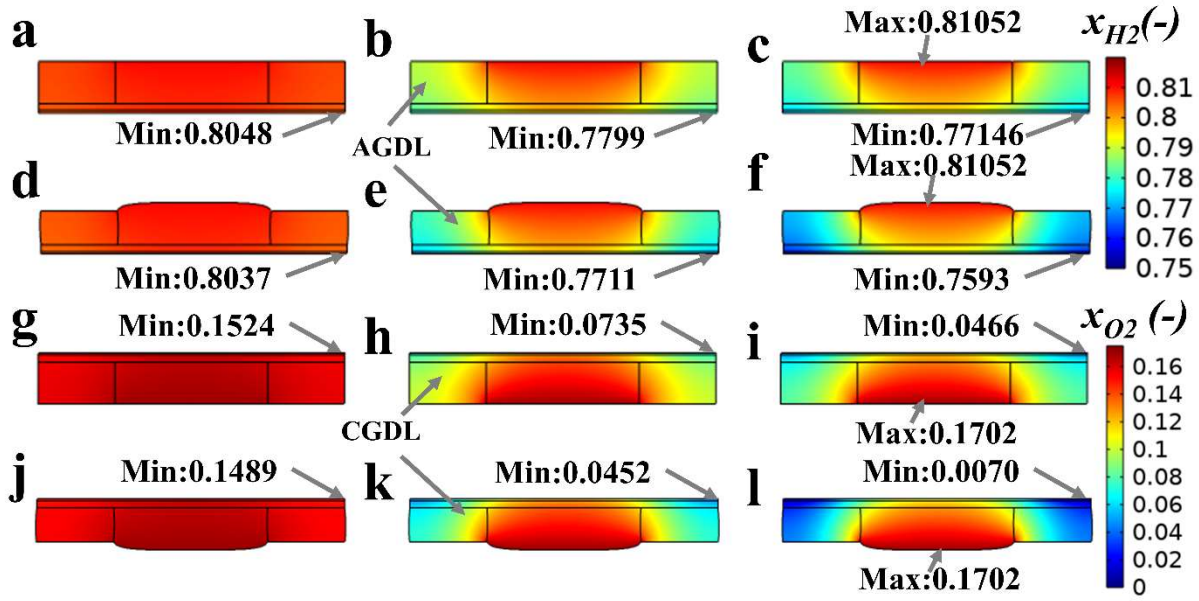

Fig. 6. Mole fraction of hydrogen and oxygen in GDM. Mole fraction of hydrogen when CR of 0 at a) 0.8 V, b) 0.6 V, and c) 0.4 V. Mole fraction of hydrogen when CR of 20% at d) 0.8 V, e) 0.6 V and f) 0.4 V. Mole fraction of oxygen when CR of 0 at g) 0.8 V, h) 0.6 V and i) 0.4 V. Mole fraction of oxygen when CR of 20% at j) 0.8 V, k) 0.6 V and l) 0.4 V.

Table 3. Parameter comparison in the different CRs.

Parameters	region	value (U=0.8 V)	value (U=0.6 V)	value (U=0.4 V)
Hydrogen distributions				
Average mole fraction	AGDM (CR=0)	0.8080	0.7972	0.7934
of hydrogen	AGDM (CR=20%)	0.8077	0.7942	0.7891
	AGDL under the rib (CR=0)	0.8071	0.7921	0.7869
	AGDL under the rib (CR=20%)	0.8062	0.7856	0.7780
Oxygen distributions				
Average mole fraction	CGDM (CR=0)	0.1622	0.1272	0.1148
of oxygen	CGDM (CR=20%)	0.1611	0.1176	0.1008

	CGDL under the rib (CR=0)	0.1592	0.1104	0.0936
	CGDL under the rib (CR=20%)	0.1564	0.0898	0.0648
Steam distributions				
Average mole fraction of steam	CGDM (CR=0)	0.1963	0.2159	0.2171
	CGDM (CR=20%)	0.1961	0.2173	0.2189
	CGDL under the rib (CR=0)	0.1985	0.2251	0.2266
	CGDL under the rib (CR=20%)	0.1990	0.2303	0.2325
Temperature distribution				
Peak temperature (℃)	MEA (CR=0)	80.2128	81.4374	82.1547
	MEA (CR=20%)	80.1860	81.3545	82.0667

3.4.2 Mole fraction of steam

Fig. 7 gives the mole fraction of steam in the MEA. The mole fraction of steam at the junction of CCL and CMPL under the ribs is higher than in other regions. This is due to the water transport produced by the electrochemical reaction to the CMPL, causing the mole fraction of steam to increase at the junction. Table 3 lists the average mole fraction of steam in CGDM, which is almost equal (<0.83%) for CR=0 and 20% within the output voltage range of this study. According to Fig. 7, at HCD (U=0.4 V), the mole fraction of steam at the CCL becomes saturated, which leads to flooding. When flooding occurs, the pores of the GDM become filled with liquid water, which hinders oxygen transportation and causes an increase in concentration loss as water accumulates. Additionally, the average mole fraction of steam in CGDL under the rib of CR=20% is 2.60% (U=0.4 V) and 2.3% (U=0.6 V) higher than that of CR=0, indicating

that the reaction rate of CR=20% is higher than that of CR=0.

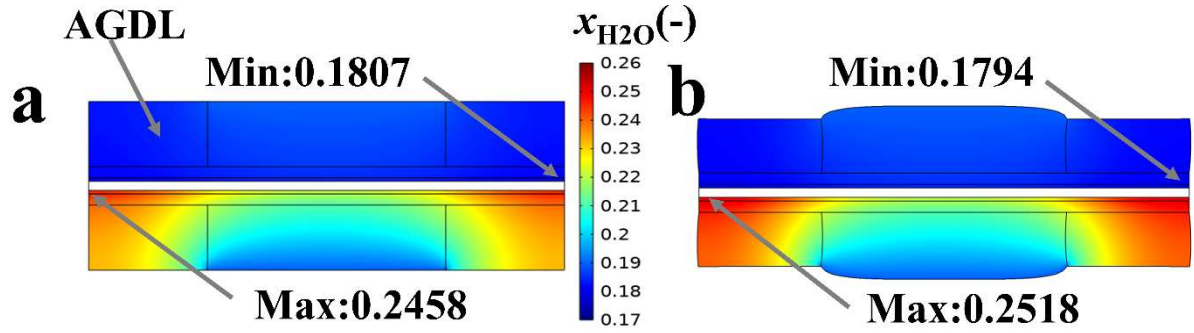

Fig. 7. Mole fraction of steam in MEA when U=0.4 V at a) CR=0 and b) CR=20%.

3.5 Temperature distributions of MEA

Fig. 8 displays the temperature distribution of MEA. According to Fig. 8a and 8b, the temperature difference between regions of MEA increases with decreasing voltage (i.e., the current density increased). At U=0.4 V, the temperature difference between regions of the MEA is 2.15 K (CR=0) and 2.07 K (CR=20%). Reducing the temperature difference improves the lifespan and stability of the PEMFC. Moreover, the temperature difference of the MEA with GDL strain is smaller than that without GDL strain, which can be attributed to two factors: 1) a shorter path length of GDL-c compared to GDL-uc, and 2) a higher thermal conductivity of GDL-c resulting in better heat transfer performance.

Fig. 8b, 8c, 8e, and 8f present the temperature distribution at the edge and center of the MEA. According to Fig. 8b and 8e, the temperature gradient of GDL-c is lower than that of GDL-uc due to the lower thermal resistance of GDL-c compared to GDL-uc. The compressed region's thermal resistance remains unchanged (Fig. 8c and 8f). Furthermore, Table 3 lists the peak temperature of the MEA, which decreases as the CR increases. Additionally, the temperature

difference for CR=20% is 12.59% (U=0.8 V), 5.77% (U=0.6 V), and 4.08% (U=0.4 V) lower than that of CR=0, indicating an improved heat dissipation performance of the MEA through GDL compression. This lower temperature difference resulting from GDL compression is beneficial for preventing membrane drying caused by high temperatures and improving PEM wetting.

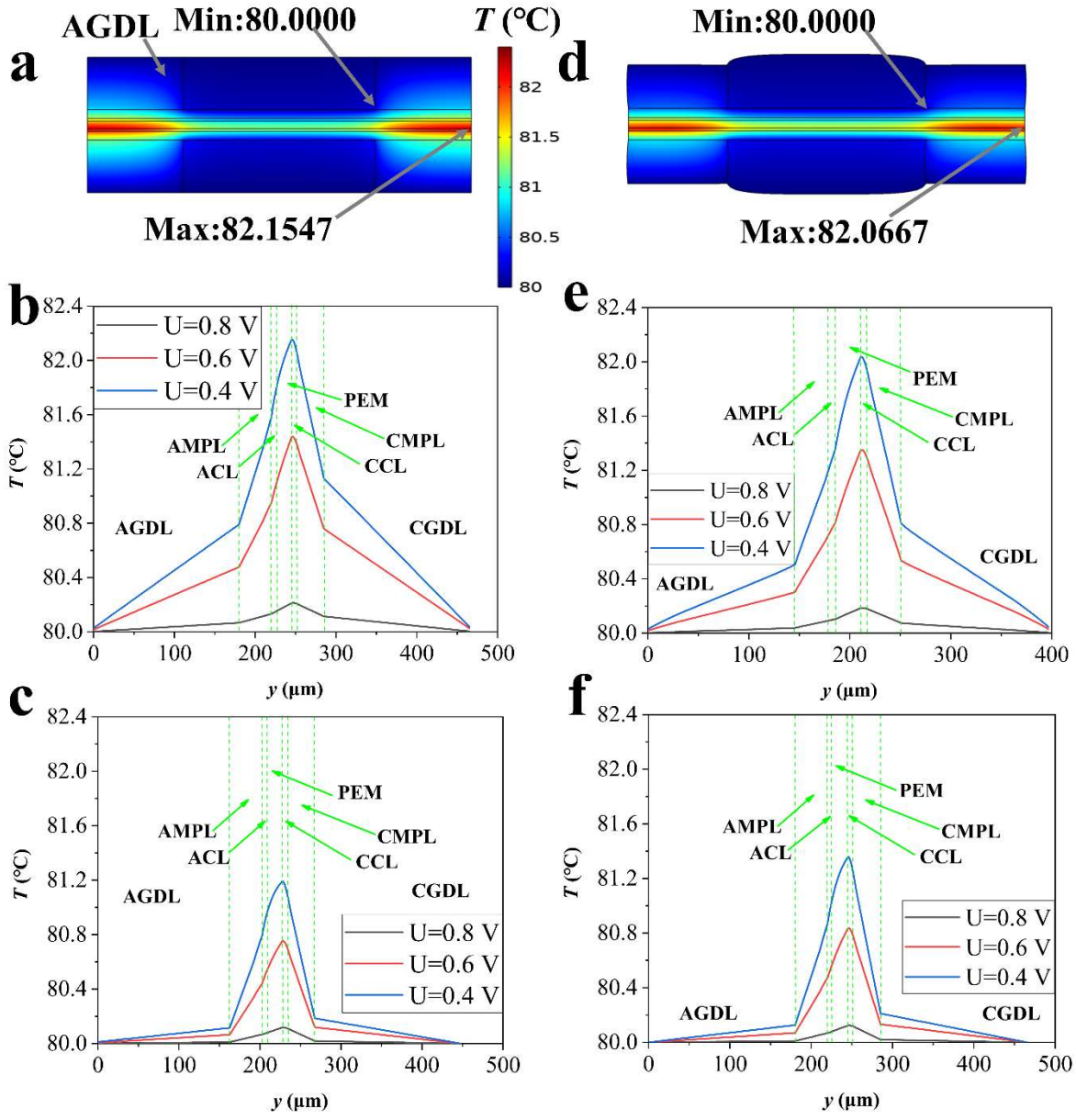

Fig. 8. Temperature distribution of MEA at a) CR=0 and b) CR=20%. Temperature distribution

in Line 1 (under the rib) of the MEA b) CR=0 and e) CR=20%. Temperature distribution in Line 1 (under the GC) of the MEA c) CR=0 and f) CR=20%.

4. Conclusions

To decrease the deviation between simulation and experiment from effective proton conductivity shifts during PEMFC assembly, the reference proton conductivity was corrected in this study. The validity of the proposed model was established through comparison with experimental data. The deviation, polarization curve, effective proton conductivity, and water content of PEM from the proposed and traditional model were compared. The distribution of gas species and temperature were investigated in this study by simulating the CR of GDL using the proposed model. The main conclusions were summarized as follows.

- The deviation of the proposed and traditional model with experimental were 10.44% and 2.25%, respectively. The peak power densities of the proposed and traditional models were 7466.6 and 6611.2 W m^{-2}, respectively, when the optimal CR was 20%. The average water content and effective proton conductivity of PEM of the proposed model were 34.29% and 41.45% higher than that of the traditional model, respectively, indicating that the proton transfer was increased. Therefore, in the prediction of the output performance of PEMFC, the proposed model was more reliable than the traditional model.
- The relationships between the output performance of PEMFC and CR of GDL were revealed. The optimal CR of this study was 20%. The water content within PEM was substantially influenced by the oxygen distribution in GDM (12.20%). At U=0.4 V, the membrane drying region for CR=0 and 20% were 46.0% and 43.2%, respectively. As a

result, the membrane drying zone was decreased by the deformed GDL, which increased the ionomer conductivity of PEM. In addition, the peak power density was increased from 6673.3 to 7466.6 W m^{-2} when the CR was increased from 0 to 20%, indicating that the output performance of PEMFC was increased by the deformed GDL.

- A considerable challenge is faced by the precise simulation of PEMFC due to the fewer experimental data on ionomer conductivity. Therefore, developing in-situ characterization technologies for ionomer conductivity in PEM is an important step toward advancing the development of PEMFC technology.

Acknowledgement

The work was financially supported by National Key Research and Development Plan (Grant No. 2022YFE0198800) and Science and Technology Planning Project of Guangdong Province (Grant No. 2021A0505030065).

Nomenclature

Symbols	Meaning (units)
$\Delta\phi_0$	Reversible potential (V)
ΔG	Change in Gibbs free energy ($J\ mol^{-1}$)
F	Faraday constant ($C\ mol^{-1}$)
p_{H2}	Partial pressure of hydrogen (Pa)
p_{O2}	Partial pressure of oxygen (Pa)
p_{ref}	Gas reference pressure (Pa)
R	Ideal-gas constant ($J\ mol^{-1}\ K^{-1}$)
ΔH	Enthalpy change ($J\ mol^{-1}$)
T	Temperature (K)
i_{an}/i_{cath}	Anode/cathode electrochemical reaction rate ($A\ m^{-3}$)
$i_{0,an}/i_{0,cath}$	Anode/cathode exchange current density ($A\ m^{-2}$)
a_{an}/a_{cath}	Anode/cathode active specific surface region (m^{-1})
η	Activation overpotential (V)
ϕ_e/ϕ_p	Electric potential of the electron/proton phase (V)
$p_{H_2}/p_{O_2}/p_{H_2O}$	Partial pressure of hydrogen/oxygen/steam (Pa)
RH	Relative humidity
p_{sat}	Saturated vapor pressure of water (Pa)

μ	Dynamic viscosity of water ($Pa\ \ s$)
σ_e/σ_p	Electron/proton conductivity ($S\ \ m^{-1}$)
$\sigma_{p,ref}$	Reference proton conductivity (S m^{-1})
S_e/S_p	Electron/proton reaction rate ($A\ \ m^{-3}$)
ε_i	Ionomer content
f	Volume fraction of water in the ionomer
λ	Water content in the ionomer
V_w	Equivalent volume of dry membrane ($m^3\ \ mol^{-1}$)
V_w	Molar volume of liquid water ($m^3\ \ mol^{-1}$)
D_λ	Diffusivity of water in ionomers ($m^2\ \ s^{-1}$)
ξ	Electroosmotic resistance coefficient
S_λ	Reaction rate of dissolved water ($mol\ \ m^{-3}\ \ s^{-1}$)
k	Thermal conductivity ($W\ \ m^{-1}\ \ K^{-1}$)
S_T	Heat source ($W\ \ m^{-3}$)
C	Total Interstitial Gas Concentration ($mol\ \ m^{-3}$)
D_{sp}	Fick's diffusion coefficients of different gases ($m^2\ \ s^{-1}$)
x_{sp}	Mole fraction of different gases
ϵ_p	Solid porosity
τ	Tortuosity
s	Saturation of liquid water
$D_{sp,ref}$	Reference Fick diffusion coefficients for different gases ($m^2\ \ s^{-1}$)
p	Total pressure of mixed gas (Pa)
κ	Hydraulic permeability (m^2)
p_c	Capillary pressure (Pa)
S_s	Reaction rate of liquid water ($mol\ \ m^{-3}\ \ s^{-1}$)
κ_{abs}	Intrinsic permeability of porous media (m^2)
s_{red}	Converted liquid water saturation
L_{cl}	Thickness of CL (m)
ϵ_{cl}	Porosity of CL
S_F	Total reaction rate ($mol\ \ m^{-3}\ \ s^{-1}$)
P	First Piola–Kirchhoff stress (Pa)
F	Deformation gradient tensor (/)
F_v	Volume force vector (N m^{-3})
I	Unit matrix (/)
u	Displacement field (m)
S	Second Piola–Kirchhoff stress (Pa)
S_{inel}	Inelastic stress tensor (Pa)
W_s	Strain energy density (J m^{-3})
σ	Cauchy stress (Pa)
J	Elastic volume ratio (/)
ε	Elastic Green-Lagrange strain (/)
J_{el}	Elastic volumetric deformation (/)
μ_l	Lamé parameters (Pa)

λ_l	Lamé parameters (Pa)
I_1	First invariant of the elastic right Cauchy–Green deformation tensor (/)

Reference

[1] Cullen DA, Neyerlin KC, Ahluwalia RK, Mukundan R, More KL, Borup RL, et al. New roads and challenges for fuel cells in heavy-duty transportation. Nature Energy 2021;6:462–74. https://doi.org/10.1038/s41560-021-00775-z.

[2] Jiao K, Xuan J, Du Q, Bao Z, Xie B, Wang B, et al. Designing the next generation of proton-exchange membrane fuel cells. Nature 2021;595:361–9. https://doi.org/10.1038/s41586-021-03482-7.

[3] Shi Q, Feng C, Ming P, Tang F, Zhang C. Compressive stress and its impact on the gas diffusion layer: A review. International Journal of Hydrogen Energy 2022;47:3994–4009. https://doi.org/10.1016/j.ijhydene.2021.10.058.

[4] Zhang H, Rahman MA, Mojica F, Sui P, Chuang PA. A comprehensive two-phase proton exchange membrane fuel cell model coupled with anisotropic properties and mechanical deformation of the gas diffusion layer. Electrochimica Acta 2021;382:138273. https://doi.org/10.1016/j.electacta.2021.138273.

[5] Pan Y, Wang H, Brandon NP. Gas diffusion layer degradation in proton exchange membrane fuel cells: Mechanisms, characterization techniques and modelling approaches. Journal of Power Sources 2021;513:230560. https://doi.org/10.1016/j.jpowsour.2021.230560.

[6] Zhu L, Zhang H, Xiao L, Bazylak A, Gao X, Sui P-C. Pore-scale modeling of gas diffusion layers: Effects of compression on transport properties. Journal of Power Sources 2021;496:229822. https://doi.org/10.1016/j.jpowsour.2021.229822.

[7] Vetter R, Schumacher JO. Free open reference implementation of a two-phase PEM fuel cell model. Computer Physics Communications 2019;234:223–34. https://doi.org/10.1016/j.cpc.2018.07.023.

[8] Görgün H, Arcak M, Barbir F. An algorithm for estimation of membrane water content in PEM fuel cells. Journal of Power Sources 2006;157:389–94. https://doi.org/10.1016/j.jpowsour.2005.07.053.

[9] Kulkarni N, Cho JIS, Jervis R, Roberts EPL, Francesco I, Kok MDR, et al. The effect of non-uniform compression on the performance of polymer electrolyte fuel cells. Journal of Power Sources 2022;521:230973. https://doi.org/10.1016/j.jpowsour.2021.230973.

[10] Chen G, Xu Q, Xuan J, Liu J, Fu Q, Shi W, et al. Numerical study of inhomogeneous deformation of gas diffusion layers on proton exchange membrane fuel cells performance. Journal of Energy Storage 2021;44:103486. https://doi.org/10.1016/j.est.2021.103486.

[11] Zhang X, Yang J, Ma X, Zhuge W, Shuai S. Modelling and analysis on effects of penetration of microporous layer into gas diffusion layer in PEM fuel cells: Focusing on mass transport. Energy 2022;254:124103. https://doi.org/10.1016/j.energy.2022.124103.

[12] Yu R, Guo H, Chen H, Ye F. Influence of different parameters on PEM fuel cell output power: A three-dimensional simulation using agglomerate model. Energy Conversion and Management 2023;280:116845. https://doi.org/10.1016/j.enconman.2023.116845.

[13] Afrasiab H, Davoodi KH, Barzegari MM, Gholami M, Hassani A. A novel constitutive stress-strain law for compressive deformation of the gas diffusion layer. International Journal

of Hydrogen Energy 2022;47:32167–80. https://doi.org/10.1016/j.ijhydene.2022.07.127.
[14] Kanchan BK, Randive P, Pati S. Implications of non-uniform porosity distribution in gas diffusion layer on the performance of a high temperature PEM fuel cell. International Journal of Hydrogen Energy 2021;46:18571–88. https://doi.org/10.1016/j.ijhydene.2021.03.010.
[15] Xia L, Ni M, He Q, Xu Q, Cheng C. Optimization of gas diffusion layer in high temperature PEMFC with the focuses on thickness and porosity. Applied Energy 2021;300:117357. https://doi.org/10.1016/j.apenergy.2021.117357.
[16] Yim S-D, Kim B-J, Sohn Y-J, Yoon Y-G, Park G-G, Lee W-Y, et al. The influence of stack clamping pressure on the performance of PEM fuel cell stack. Current Applied Physics 2010;10:S59–61. https://doi.org/10.1016/j.cap.2009.11.042.
[17] Senthil Velan V, Velayutham G, Rajalakshmi N, Dhathathreyan KS. Influence of compressive stress on the pore structure of carbon cloth based gas diffusion layer investigated by capillary flow porometry. International Journal of Hydrogen Energy 2014;39:1752–9. https://doi.org/10.1016/j.ijhydene.2013.11.038.
[18] Molaeimanesh GR, Nazemian M. Investigation of GDL compression effects on the performance of a PEM fuel cell cathode by lattice Boltzmann method. Journal of Power Sources 2017;359:494–506. https://doi.org/10.1016/j.jpowsour.2017.05.078.
[19] Athanasaki G, Jayakumar A, Kannan AM. Gas diffusion layers for PEM fuel cells: Materials, properties and manufacturing – A review. International Journal of Hydrogen Energy 2023;48:2294–313. https://doi.org/10.1016/j.ijhydene.2022.10.058.
[20] Simon C, Hasché F, Gasteiger HA. Influence of the Gas Diffusion Layer Compression on the Oxygen Transport in PEM Fuel Cells at High Water Saturation Levels. Journal of The Electrochemical Society 2017;164:F591–9. https://doi.org/10.1149/2.0691706jes.
[21] Wang H, Yang G, Li S, Shen Q, Li Y, Wang R. Pore-Scale Modeling of Liquid Water Transport in Compressed Gas Diffusion Layer of Proton Exchange Membrane Fuel Cells Considering Fiber Anisotropy. Membranes 2023;13:559. https://doi.org/10.3390/membranes13060559.
[22] Song K, Wang Y, Ding Y, Xu H, Mueller-Welt P, Stuermlinger T, et al. Assembly techniques for proton exchange membrane fuel cell stack: A literature review. Renewable and Sustainable Energy Reviews 2022;153:111777. https://doi.org/10.1016/j.rser.2021.111777.
[23] Grimm M, Hellmann M, Kemmer H, Kabelac S. Interaction of cell flow directions and performance in PEM fuel cell systems following an anode based water management approach. Journal of Power Sources 2023;580:233270. https://doi.org/10.1016/j.jpowsour.2023.233270.
[24] Yan X, Lin C, Zheng Z, Chen J, Wei G, Zhang J. Effect of clamping pressure on liquid-cooled PEMFC stack performance considering inhomogeneous gas diffusion layer compression. Applied Energy 2020;258:114073. https://doi.org/10.1016/j.apenergy.2019.114073.
[25] Zenyuk IV, Parkinson DY, Connolly LG, Weber AZ. Gas-diffusion-layer structural properties under compression via X-ray tomography. Journal of Power Sources 2016;328:364–76. https://doi.org/10.1016/j.jpowsour.2016.08.020.
[26] O'Hayre RP, Cha S-W, Colella WG, Prinz FB. Fuel cell fundamentals. Third edition. Hoboken, New Jersey: John Wiley & Sons Inc; 2016.
[27] Springer TE, Zawodzinski TA, Gottesfeld S. Polymer Electrolyte Fuel Cell Model. Journal of The Electrochemical Society 1991;138:2334–42. https://doi.org/10.1149/1.2085971.
[28] Lampinen M, Fomino M. Analysis of different energy scales in chemical thermodynamics

and estimation of free energy and enthalpy changes for half cell reactions. Acta Polytechnica Scandinavica 1993:45.
[29] Maldonado L, Perrin J-C, Dillet J, Lottin O. Characterization of polymer electrolyte Nafion membranes: Influence of temperature, heat treatment and drying protocol on sorption and transport properties. Journal of Membrane Science 2012;389:43–56. https://doi.org/10.1016/j.memsci.2011.10.014.
[30] Slade S, Campbell SA, Ralph TR, Walsh FC. Ionic Conductivity of an Extruded Nafion 1100 EW Series of Membranes. Journal of The Electrochemical Society 2002;149:A1556. https://doi.org/10.1149/1.1517281.
[31] Harilal, Shukla A, Chandra Ghosh P, Jana T. Copolymers of Pyridine-bridged polybenzimidazole for the use in high temperature PEM fuel cell. European Polymer Journal 2022;177:111445. https://doi.org/10.1016/j.eurpolymj.2022.111445.
[32] A comprehensive review on the proton conductivity of proton exchange membranes (PEMs) under anhydrous conditions: Proton conductivity upper bound. International Journal of Hydrogen Energy 2021;46:34413–37. https://doi.org/10.1016/j.ijhydene.2021.08.015.
[33] Peron J, Mani A, Zhao X, Edwards D, Adachi M, Soboleva T, et al. Properties of Nafion® NR-211 membranes for PEMFCs. Journal of Membrane Science 2010;356:44–51. https://doi.org/10.1016/j.memsci.2010.03.025.
[34] Khetabi EM, Bouziane K, Zamel N, François X, Meyer Y, Candusso D. Effects of mechanical compression on the performance of polymer electrolyte fuel cells and analysis through in-situ characterisation techniques - A review. Journal of Power Sources 2019;424:8–26. https://doi.org/10.1016/j.jpowsour.2019.03.071.
[35] Ge J, Higier A, Liu H. Effect of gas diffusion layer compression on PEM fuel cell performance. Journal of Power Sources 2006;159:922–7. https://doi.org/10.1016/j.jpowsour.2005.11.069.
[36] Leng Y, Yao H, Yang D, Li B, Ming P, Zhang C. The influences of gas diffusion layer material models and parameters on mechanical analysis of proton exchange membrane fuel cell. Fuel Cells 2021;21:373–89. https://doi.org/10.1002/fuce.202100068.
[37] Zhang T, Li J, Li Q, Yu M, Sun H. Combination effects of flow field structure and assembly force on performance of high temperature proton exchange membrane fuel cells. International Journal of Energy Research 2021;45:7903–17. https://doi.org/10.1002/er.6374.
[38] Green DW, Southard MZ, editors. Perry's chemical engineers' handbook. Ninth edition, 85th anniversary edition. New York: McGraw Hill Education; 2019.
[39] Kusoglu A, Weber AZ. New Insights into Perfluorinated Sulfonic-Acid Ionomers. Chemical Reviews 2017;117:987–1104. https://doi.org/10.1021/acs.chemrev.6b00159.
[40] Neyerlin KC, Gu W, Jorne J, Gasteiger HA. Determination of Catalyst Unique Parameters for the Oxygen Reduction Reaction in a PEMFC. Journal of The Electrochemical Society 2006;153:A1955. https://doi.org/10.1149/1.2266294.
[41] Wang Y, Liu T, Sun H, He W, Fan Y, Wang S. Investigation of dry ionomer volume fraction in cathode catalyst layer under different relative humilities and nonuniform ionomer-gradient distributions for PEM fuel cells. Electrochimica Acta 2020;353:136491. https://doi.org/10.1016/j.electacta.2020.136491.
[42] Ge S, Li X, Yi B, Hsing I-M. Absorption, Desorption, and Transport of Water in Polymer Electrolyte Membranes for Fuel Cells. Journal of The Electrochemical Society 2005;152:A1149.

https://doi.org/10.1149/1.1899263.